International Journal of Mechanical Sciences 312 (2026) 111251

Contents lists available at ScienceDirect

International Journal of Mechanical Sciences

journal homepage: www.elsevier.com/locate/ijmecsci

Regression-guided computational design of auxetic scaffolds for soft tissue applications

Óscar Lecina-Tejero [a], Jesús Asín [b], Jesús Cuartero [c], María Ángeles Pérez [a], Carlos Borau [a],*

[a] Multiscale in Mechanical and Biological Engineering, Aragon Institute of Engineering Research (I3A), School of Engineering and Architecture, University of Zaragoza, Zaragoza, 50018, Aragon, Spain
[b] Department of Statistical Methods, University of Zaragoza, Zaragoza, 50018, Aragon, Spain
[c] Department of Mechanical Engineering, University of Zaragoza, Zaragoza, 50018, Aragon, Spain

ARTICLE INFO

Dataset link: https://github.com/olecina/MEW-FEM-AuxeticDesigner

Keywords:
Auxetic scaffolds
Soft tissue engineering
Mechanical behavior
Computational design
Regression-based predictive modeling

ABSTRACT

The mechanical performance of tissue-engineered scaffolds plays a critical role in their effectiveness for regenerative medicine. While auxetic metamaterials offer tunable mechanical behavior ideal for soft tissues, their design typically relies on inefficient, iterative trial-and-error processes. To address this limitation, this study presents an integrated computational framework for the inverse design of auxetic scaffolds. By combining Finite Element Method (FEM) simulations with regression-based models, we developed accurate predictive models capable of mapping microstructural parameters directly to macroscopic mechanical responses. This data-driven approach allowed for the rigorous optimization of four distinct auxetic architectures to replicate the complex, non-linear anisotropic properties of human skin, achieving strong agreement with literature targets. A primary contribution of this work is the development of a user-friendly software tool that integrates this pipeline. The tool allows users to input target mechanical properties and automatically generates optimized, fabrication-ready designs (including custom MEW G-code), effectively bridging the gap between theoretical metamaterial optimization and practical clinical application. This methodology supports robust, patient-specific scaffold development, significantly advancing the capabilities of soft tissue engineering.

1. Introduction

Tissue engineering and advanced manufacturing techniques have revolutionized wound healing by developing advanced constructs that mimic the properties of the native tissue extracellular matrix, enabling improved cell proliferation and the regeneration of more complex tissue structures [1]. While traditional tissue engineering scaffolds face challenges in mechanical adaptability, auxetic metamaterials emerge as a promising solution due to their enhanced conformability to dynamic mechanical environments and tunable, design-induced mechanical properties [2,3].

Auxetic metamaterials are characterized by a negative Poisson's ratio, meaning they expand laterally when stretched. This unique property allows them to accommodate significant biaxial deformation while maintaining stable internal stress and adapting their morphology effectively to irregular surfaces [4]. These metamaterials have demonstrated significant potential in a wide range of biomedical applications [5–7] including bone tissue engineering [8,9], vascular grafts [10–12], and cardiac patches [13–16]. Recent studies have highlighted the ability of fibrous scaffolds architected with auxetic meta-structures to mimic the native strain-stiffening behavior of soft tissues [17,18], which have promoted their use in multiple soft tissue engineering applications [19–23]. Mirani et al. [17] proposed a combined approach of computational modeling and 3D printing to fabricate tissue engineering scaffolds with auxetic designs mimicking the mechanical behavior of porcine pericardium and cardiac valves, while Chansoria et al. [23] investigated the production of hydrogel patches with auxetic geometries adapted to the behavior of dynamic organs, such as lungs, heart, or skin.

In the context of soft tissue engineering, understanding the mechanical behavior of the native tissue is essential for designing effective biomimetic scaffolds [24–26]. For example, human skin exhibits a nonlinear and anisotropic behavior [27–29] which several computational and experimental studies have attempted to replicate using synthetic substitutes [30–34]. However, such substitutes fall short to replicate

---

* Corresponding author at: Multiscale in Mechanical and Biological Engineering, Aragon Institute of Engineering Research (I3A), School of Engineering and Architecture, University of Zaragoza, Zaragoza, 50018, Aragon, Spain.

E-mail address: cborau@unizar.es (C. Borau).

https://doi.org/10.1016/j.ijmecsci.2026.111251
Received 2 June 2025; Received in revised form 12 December 2025; Accepted 12 January 2026

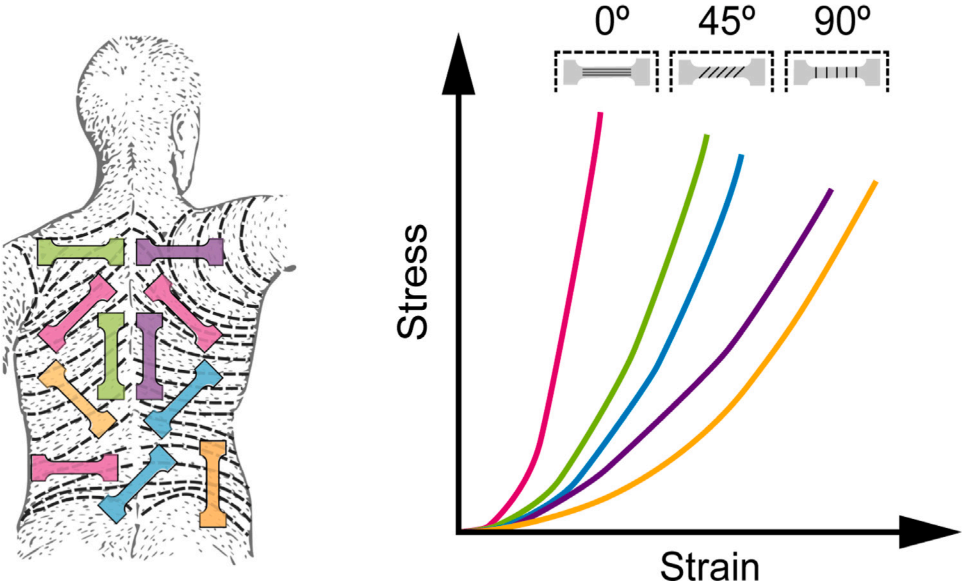

Fig. 1. Anatomical mapping and anisotropic mechanical characterization of human skin. The schematic illustrates the extraction sites of skin samples from the human back relative to the orientation of Langer lines (collagen fiber alignment). The plot displays representative stress–strain curves for samples tested at 0° (parallel), 45°, and 90° (perpendicular) to the Langer lines. Note the characteristic non-linear "J-shaped" behavior and the significant anisotropy, where samples aligned with Langer lines (0°) exhibit higher stiffness compared to perpendicular ones (90°). These mechanical profiles serve as the target properties for the scaffold optimization in this study.
Source: Figure adapted from [41].

the high variability of the skin behavior, influenced by multiple factors including gender, age, body region, thickness, or collagen fiber orientation [35–40]. For instance, Fig. 1, adapted from the research of Annaidh et al. [41], illustrates these variations. In their study, samples of human back skin were extracted from different regions of the back and aligned distinctly relative to their local Langer lines, which are the principal directions of tension in the skin [42–44]. The mechanical characterization of these samples revealed variations in the mechanical behavior depending on both location and orientation.

Importantly, the mechanical performance of auxetic metamaterials depends on their design. By controlling the parameters of their microstructural geometry, it is possible to tailor the mechanical properties of the scaffolds to specific functional requirements [2]. Melt electro-writing (MEW) has established itself as a high-resolution additive manufacturing technique capable of depositing fibers with micrometer precision [45,46]. This technology has been extensively utilized to fabricate complex scaffold microarchitectures with controlled anisotropy [47,48], enabling the precise realization of theoretically designed metamaterials [49–52].

Computational analysis using the finite element method (FEM) is a widely adopted tool for structural analysis and design optimization as it enables testing multiple configurations involving geometry, material properties, assemblies, and boundary conditions [53–55]. This allows evaluation of structural performance prior to fabrication, saving time, material, and economic resources. However, FEM analysis of intricate and complex models can incur substantial computational costs, particularly when exploring extensive design spaces with numerous configurations [23,55,56]. This increased computational demand may slow the design process and complicate achieving precise mechanical targets. The combination of computational modeling and statistical regression is a validated approach to address these challenges [17], where experimentally validated data can be utilized to train regression models, explore multiple output predictions, and efficiently optimize the design to achieve accurate, prescribed mechanics.

In recent years, data-driven approaches and machine learning frameworks have emerged as powerful tools to accelerate the discovery and optimization of mechanical metamaterials [57–62]. Specifically, inverse design strategies leveraging deep learning and regression algorithms have been successfully applied to tailor the non-linear properties of architected metamaterials [63–65], overcoming the limitations of traditional trial-and-error methodologies [66,67].

Our work proposes an integrated predictive framework combining FEM simulations, data-driven statistical regression modeling, and computational optimization for the design of auxetic-architected microfibrous scaffolds for soft tissue engineering applications. By employing a design of experiments (DOE) strategy, a reduced number of scaffold configurations can be utilized to generate a representative dataset of FEM computed results. These type of simulations have been developed and experimentally validated in our previous work [68]. Regression models trained on this dataset can predict mechanical properties directly from the microstructural design parameters, decreasing the computational effort needed to explore extensive design spaces. Using experimentally obtained human skin mechanical properties (specifically, measurements from back skin samples characterized by Annaidh et al. [41]) as representative targets, this methodology enables the efficient identification of optimal auxetic microfibrous scaffold geometries tailored to patient-specific mechanical conditions. The innovation of this work is the development of an integrated and application specific-framework connecting: (i) a biologically validated auxetic scaffold family [68], (ii) mechanical characterization and reduction of its key operational parameters, and (iii) a surrogate-model-driven inverse design pipeline that enables patient-specific customization. This approach accelerates scaffold development while maintaining accuracy, making it applicable to various soft tissue engineering applications. To support practical implementation, we provide a computational tool [69] that enables users to select optimal design parameters to achieve specific mechanical behaviors.

The remainder of this paper is organized as follows: Section 2 details the computational framework, describing the FEM setup, the design of experiments, and the regression methodologies employed. Section 3 presents the results of the sensitivity analysis, the predictive accuracy of the models, and the validation against literature data. Section 4 discusses the implications of these findings for scaffold design and introduces the developed software tool. Finally, Section 5 summarizes the main conclusions and outlines future research directions.

2. Materials and methods

The work presented here follows an integrated computational workflow designed to predict and optimize the mechanical behavior of auxetic fiber-based scaffolds for soft tissue engineering. The process begins by defining four auxetic geometries, each parameterized to allow systematic variation in scaffold design. A structured DOE approach was employed to generate a representative set of scaffold configurations by varying key geometric parameters. FEM simulations were then performed on these configurations to assess their mechanical behavior under biaxial loading conditions. The resulting data were used to train statistical models capable of predicting scaffold effective stiffness and strain as a function of design parameters. Finally, optimization techniques were evaluated and applied to identify scaffold geometries that best match specific mechanical targets. This framework enables the rapid and reliable selection of scaffold designs tailored to desired mechanical performance.

2.1. Selected auxetic geometries

This study builds upon the framework established in our previous work [68], where auxetic micro-fibrous scaffolds were fabricated via MEW using polycaprolactone (PCL), a synthetic, FDA-approved biopolymer widely utilized in tissue engineering. In that prior study, we characterized the mechanical behavior of the PCL scaffolds both experimentally and numerically, and validated their cytocompatibility for biological applications. MEW was selected as the manufacturing technique because it provides precise control over microfiber deposition during the printing process, allowing for the implementation of specific printing paths to create intricate fibrous microstructures [45, 46]. Consequently, all scaffold geometries presented in this work are specifically designed for fabrication by MEW [70–72].

We selected four re-entrant auxetic designs to define the microstructure of the scaffolds based on their suitability for MEW fabrication, designated as *H-cell* (*HCELL*), *S-regular* (*SREG*), *S-inverted* (*SINV*), and *S-triangular* (*STRI*). These designs were characterized by basic unit cells and parameterized as illustrated in Fig. 2 to investigate the influence of geometric variations in auxetic architectures on the mechanical response of the scaffolds. The parameters "a" and "b" were defined to capture geometric variations in fiber layout, while the parameter "d" controlled the fiber diameter. The parameters "xr", "yr", and "zr" defined the scaffold's physical dimensions (i.e., the number of unit cell repetitions in the x and y directions, and the number of stacked layers in the z direction).

2.2. Design of experiments

The design space was explored using a structured DOE strategy that systematically covered the lower, medium, and upper regions of the design space for the selected geometry parameters, which were "a", "b", "d", and "yr". Given that this structured grid is designed to define the boundaries and center of the parameter space, the entire dataset was utilized for model training to preserve interpolation accuracy, while predictive performance was evaluated on unseen data during the subsequent optimization phase. Among them, parameter "a" played a central role, as it determined the overall scale of the auxetic geometry and, consequently, the size of the scaffold. To ensure a reduced scaffold scale suitable for tissue engineering applications, its values were constrained between 100 and 300 μm. Smaller "a" values may lead to fabrication challenges and compromised structural fidelity, while larger values could result in oversized features unsuitable for scaffold considerations.

It is important to note that parameter "b" was defined relative to parameter "a" to address design scalability and to comply with the geometric constraints of each auxetic design. Specifically, for the *SREG* and *STRI* designs, parameter "b" was established as 0.5, 1, and 1.5 times the value of "a", since higher ratios would lead to fiber overlaps and distortions that compromise the auxetic effect, and smaller values would result in almost straight fibers, not demonstrating any auxetic performance. Therefore, 1.5 was considered the upper limit for the "b" to "a" ratio ("rba", Eq. (1)) across the designs. For the *SINV* design, the same geometric constraints applied, but in this case it restricted the parameter "b" to not exceed "a". As a result, the "rba" ratios investigated for this design were limited to 0.25, 0.5, and 0.75. In contrast, the *HCELL* design imposed no such restrictions on this ratio, allowing the use of the same range applied in the *SREG* and *STRI* designs.

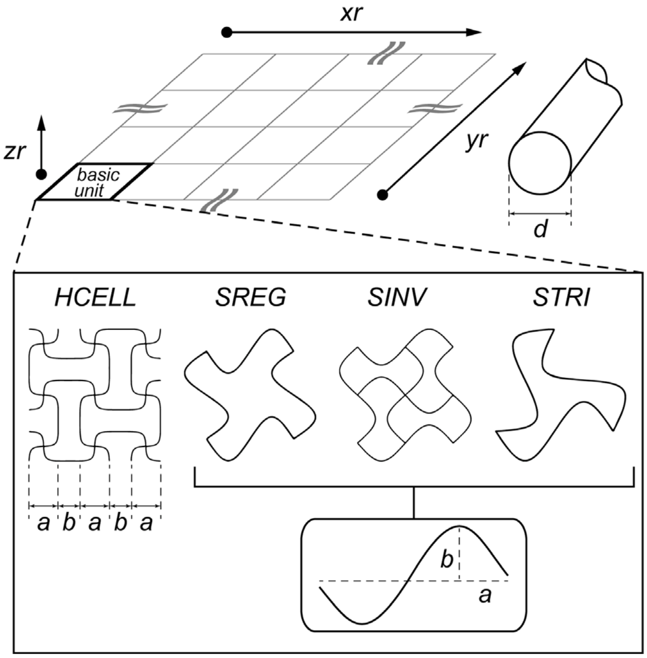

Fig. 2. Parametric definition of auxetic unit cells and scaffold architecture. The study evaluates four distinct re-entrant auxetic topologies: *H-cell* (*HCELL*), *S-regular* (*SREG*), *S-inverted* (*SINV*), and *S-triangular* (*STRI*). The schematic illustrates the key geometric parameters utilized to define the design space. Parameters "a" and "b" determine the characteristic dimensions and aspect ratio of the individual unit cells. Parameter "d" corresponds to the fiber diameter. Parameters "xr", "yr", and "zr" specify the number of unit cell repetitions in the x, y, and z directions, respectively, thereby defining the macroscopic volume and aspect ratio of the scaffold. These parameters serve as the input variables for the DOE strategy.

$$rba = b/a \tag{1}$$

Parameters "d" and "yr" did not present design-specific limitations and were varied uniformly across all four designs. Specifically, "d" was evaluated between 10 and 20 μm, which are common fiber diameters obtained with MEW [68], and parameter "yr" ranged from 3 to 9 unit cell repetitions. Parameters "xr" and "zr" were fixed at values of 6 and 10, respectively, so their combination with the varying values of "yr" allowed exploration of the influence of scaffold shape aspect ratio on the mechanical behavior, while also reducing the number of required configurations.

This parameter combination ("a", "rba", "d", "yr") yielded a DOE dataset comprising 324 unique scaffold configurations, with 81 configurations per auxetic design. Table 1 summarizes the parameter values explored for the four auxetic designs.

2.3. Numerical simulations

The mechanical performance of the scaffolds was evaluated by conducting FEM-based simulations with ABAQUS software (3DS Dassault

Table 1
Summary of the auxetic designs and the values of their geometry parameters considered in the design of experiments. To maintain design consistency, parameter "*rba*" had to take different values for *SINV* design, while remaining unaltered for the other auxetic designs. The values were attributed to the parameters aiming to explore the design space, comprising both reduced scales feasible by MEW-fabrication and wider scales but without excessively increasing the features, which could lead to lose scaffold-like scales in the structures. The combination of all the possible configurations of the four designs followed this formula: $Values^{Parameters} * Designs = 3^4 * 4 = 324$, constituting a database of 324 distinct scaffold geometry configurations, with each design represented by 81 unique configurations.

Geometry parameter	Auxetic design	Lower value	Medium value	Higher value
a [μm]	*ALL*	100	200	300
rba [−]	*HCELL* *SREG* *STRI*	0.5	1	1.5
	SINV	0.25	0.5	0.75
d [μm]	*ALL*	10	15	20
yr [−]	*ALL*	3	6	9

Systems). The FEM model of the scaffolds was developed and experimentally validated on our previous work [68], where FEM simulations reproduced the biaxial tensile behavior of the MEW-fabricated auxetic scaffolds. The FEM model replicated the fibrous structure of the scaffolds with 3D beam linear elements (B31) with circular cross-sections, implemented a elastic–plastic constitutive law for PCL following the behavior observed in the performed experimental characterization of PCL bulk material, with an elastic modulus of 100 MPa up to a yield stress of 12 MPa followed by a progressively increased stiffness in the plastic region. Mesh controls were applied over the length-to-diameter ratio of the elements (>10) to ensure appropriate element size while maintaining fidelity to fiber architecture, and node coupling was utilized to interconnect the superposed element layers of the scaffold model. Geometric nonlinearity (large deformation theory) was enabled to capture the reorientation and unfolding of the elements during the tensile process. FEM simulations reproduced the mechanical conditions of the scaffolds during biaxial tensile tests based on control over applied displacement and utilizing a quarter-symmetry model of the scaffolds to reduce computational costs. The Python-based ABAQUS scripts utilized to generate the FEM models are publicly available [69,73].

Although Poisson's ratio is a defining characteristic of auxetic metamaterials, it was not extracted from these specific FEM simulations due to the boundary conditions of the equibiaxial tensile tests. Since symmetric displacements were prescribed in both principal directions, the transverse strain was constrained, preventing the derivation of a free Poisson's ratio. Consequently, data analysis focused on identifying the state at which scaffold fibers become fully stretched, which defines the operational limit of the auxetic geometry mechanism. At that point, we measured the strain (ε_{aux}) and calculated the elastic modulus (E_{aux}). The calculation of these key variables starts by extracting nodal displacements from the stretched edges and reaction forces from the constrained edges, which allowed to obtain the effective stress (σ [kPa]) and strain (ε [μm / μm]) of the scaffolds following the procedure explained in Supp. Info (Figure S1). To consistently define the transition from the initial compliant behavior to the stiffer mechanical response, considering the variability of curve shapes, ε_{aux} was defined as the strain at which the instantaneous effective elastic modulus (i.e., the first derivative of the σ-ε curve, E [kPa]) reaches approximately half of its maximum value during the ascending phase, as represented in Fig. 3-A and Eq. (2). This relative criterion enabled robust identification of the transition point across the scaffold designs in both x- and y-directions, and the most restricting direction in each case (i.e., the one with the higher E_{aux}) was selected to characterize the scaffold behavior.

$$\varepsilon_{\text{aux}} = \varepsilon \quad \text{such that} \quad E(\varepsilon) = \frac{1}{2} E_{\max} = E_{\text{aux}} \tag{2}$$

E_{aux} and ε_{aux} have been defined in alignment with what has been previously described as the transition between "Zone 2" and "Zone 3" in studies of native soft tissues, such as porcine skin [74], where the fibrous components become fully aligned and contribute to a increase in stiffness. This analogy supports the relevance of E_{aux} and ε_{aux} as representative parameters of the mechanical behavior of the scaffolds in its load-bearing regime. These properties, initially extracted as output responses from FEM simulations, will later serve as key input variables in the operative phase of the study, guiding predictive modeling and scaffold design optimization.

2.4. Statistical modeling and optimization procedure

This stage of the methodology addresses the challenge of characterizing the relationship between the scaffold design parameters and their mechanical responses, specifically predicting E_{aux} and ε_{aux} from geometric variables such as fiber geometric disposition ("*a*" and "*rba*"), fiber diameter ("*d*"), or scaffold aspect ratio ("*yr*"). Despite the extensive DOE performed, the resulting dataset only samples a limited portion of the full parameter space, making it difficult to directly define an explicit function such as Eq. (3):

$$E_{\text{aux}} = f(a, rba, d, yr) \tag{3}$$

To overcome this limitation, statistical modeling was employed to extract signal from the data and to capture the inherent variability observed in the mechanical response curves. Regression models served two main purposes at this stage. First, they identify which design parameters influence the mechanical behavior of the scaffold, thus enabling dimensionality reduction by eliminating non-influential variables. Second, they provide prediction intervals for the responses, which define a set of possible scaffold configurations compatible with a desired target behavior.

Following the statistical modeling phase, an optimization step becomes necessary to address the inverse design problem: determining which values of the design parameters yield a target mechanical response, represented in Eq. (4):

$$E_{\text{aux}}(a_i, rba_i, d_i, yr_i) = E_{\text{aux-target}} \tag{4}$$

The inverse problem is analytically intractable due to the nonlinear and potentially multi-modal nature of the relationships between design parameters and mechanical responses. Therefore, optimization algorithms are required to explore the solution space defined by the statistical model. It is worth noting that while the inverse design strictly targets E_{aux}, surrogate models for ε_{aux} were also developed to monitor strain levels, providing a comprehensive characterization of the operational limits of the auxetic mechanism of the optimized designs.

The statistical analysis began by fitting regression models relating the FEM simulation outputs (E_{aux} and ε_{aux}) to the geometric parameters of the auxetic designs. For each design, separate regression equations were constructed for each response variable, resulting in a total of eight models. The initial formulation used in all cases included main effects, two-way interaction terms, and quadratic terms, allowing the models to capture a wide range of potential relationships and to represent linear and nonlinear trends, as well as interaction effects. This is represented in Eq. (5):

$$Y = \beta_0 + \sum_i \beta_i X_i + \sum_{i,j} \beta_{ij} X_i X_j + \sum_i \beta_{ii} X_i^2 \tag{5}$$

where Y represents either E_{aux} or ε_{aux}, depending on the model, and X_i corresponds to the scaffold design parameters ("*a*", "*rba*", "*d*", and "*yr*"). Each auxetic design is modeled independently, allowing the regression equation to reflect design-specific mechanical responses and sensitivities.

Stepwise regression was then conducted in both forward and backward directions to iteratively include or exclude predictor terms based on statistical significance (p-value < 0.05), with the Bayesian Information Criterion (BIC) used to guide model selection. This procedure was independently applied to each response variable (E_{aux}, ε_{aux}) for all four auxetic designs, yielding eight distinct regression models.

Once trained, these models functioned as surrogate predictors of the scaffold's mechanical response based on its geometric parameters. However, prediction alone does not resolve the inverse design problem: determining the input parameters that will yield a specific target mechanical behavior. To address this, an optimization framework was implemented to explore the defined design space for configurations that achieve target values (e.g., $E_{\text{aux-target}}$) while ensuring robustness against geometric variability.

Several optimization strategies were tested within the DOE-defined space, including random grid search, brute-force exploration, and genetic algorithms. Given the negligible computational cost of querying the surrogate models, adaptive grid refinement strategies were not deemed necessary; instead, high-density sampling was preferred to ensure thorough design space exploration and minimize the risk of missing optimal regions due to initial coarse sampling. Consequently, the chosen approaches focused on maximizing coverage within the constrained parameter space [75]. All optimization strategies aimed to minimize a custom loss function (Eq. (6)) that balances two critical aspects of inverse design: *predictive accuracy* and *robustness*. The first term in the equation represents the bias, that is, the mean squared error (MSE) between the average prediction and the target value, ensuring the design meets the desired mechanical response. The second term penalizes high variance among predictions, promoting *reliability* by favoring designs that are less sensitive to small perturbations in geometric parameters. This dual-objective formulation encourages scaffold configurations that are both precise and robust against variability in fabrication or parameter estimation.

$$\mathcal{L} = \frac{1}{n}\sum_{i=1}^{n}(\hat{E}_{\text{aux},i} - E_{\text{aux-target}})^2 + \frac{1}{n}\sum_{i=1}^{n}(\hat{E}_{\text{aux},i} - \bar{\hat{E}}_{\text{aux}})^2 \tag{6}$$

Here, $\mathcal{L}$ denotes the loss function to be minimized, $\hat{E}_{\text{aux},i}$ are the predictions for each design, $E_{\text{aux-target}}$ is the desired target value, and $\bar{\hat{E}}_{\text{aux}} = \frac{1}{n}\sum_{i=1}^{n}\hat{E}_{\text{aux},i}$ is the mean of the perturbed design predictions. In this formulation, i indexes each design, and n represents the total number of perturbed designs evaluated.

Details on the comparative performance of these optimization methods, and the rationale for selecting the final approach, are discussed in the Results section and Supp. Info (Table S1).

R software functions were designed to apply the random grid search method [76], which began with a seed-based sampling of geometric configurations randomly drawn from the DOE space. This seed set was expanded to a pool of up to 5000 unique configurations, each evaluated using the objective function (Eq. (6)). Sensitivity analysis indicated that the choice of random seed and sample size had minimal impact on the overall outcomes. In contrast, brute-force analysis exhaustively evaluated approximately 770,000 configurations, generated by combining 100 evenly spaces values of "a" and "rba" with all feasible integer values of "d" and "yr". Lastly, a genetic algorithm was implemented using the GA [77] package in R, applying evolutionary operations such as selection, crossover, and mutation to iteratively converge toward optimal solutions within the parameter space.

3. Results

The following section presents the outcomes of the computational optimization process. We first analyze the influence of geometric parameters on the mechanical properties through FEM simulations. Next, we evaluate the accuracy of the regression models in predicting the auxetic behavior and stiffness of the scaffolds. Finally, the optimized designs are validated against target mechanical properties of human soft tissues, demonstrating the efficacy of the proposed inverse design framework and the software tool developed to integrate the entire design process and facilitate the translation of the methodology to specific applications.

3.1. FEM simulations demonstrate the design-dependent, non-linear mechanical behavior of auxetic scaffolds

The 324 FEM models of auxetic microfibrous scaffolds were simulated replicating the conditions of biaxial tensile testing described in our previous work [68]. Panels (a-d) of Fig. 3 present the simulated stress–strain relationships of the four auxetic geometry designs, with the curves grouped according to distinguishable patterns to enhance clarity.

The FEM simulation results reveal that auxetic scaffolds exhibit a non-linear mechanical response, commonly referred to as "J-shaped" behavior, characteristic of soft tissues. This begins with an initial low stiffness (toe region), which progressively increases with stretching (heel region) until reaching a linear region, corresponding to the full expansion and alignment of the scaffold fibers along the loading direction. This non-linearity does not arise from fiber material behavior but from geometric non-linearity, which is the primary source of mechanical non-linearity in auxetic structures. The non-linear response is driven by the architectural unfolding, reorientation, and large rotational deformations inherent to these auxetic geometries under tension. The *HCELL* and *SINV* designs display two groups of curves (Fig. 3-(a,c)), both exhibiting low strain values, indicating a limited deformation capacity. However, the higher stress values observed in the *SINV* curves clearly demonstrate a stiffer mechanical response. In contrast, the *SREG* and *STRI* designs show three groups of curves reaching higher strain values (Fig. 3-(b,d)), suggesting greater deformation capacity. Notably, the low stress values associated with the *SREG* design reflect the softest mechanical behavior among the four auxetic geometries. These findings underscore the mechanical versatility of the auxetic scaffolds, where variations in design and geometry can yield a broad spectrum of flexible or resilient mechanical responses.

Both inter-design and intra-design variability of E_{aux} and ε_{aux} were analyzed to better understand the mechanical properties that auxetic microfibrous scaffolds can exhibit depending on their design and geometric configuration. Fig. 3-(e) shows the kernel density estimations (KDE) of E_{aux} and ε_{aux} across the four auxetic scaffold designs, highlighting both the overall trends and the variability associated with each design.

The *HCELL* design exhibits a narrow, well-defined distribution in both variables, with ε_{aux} values ranging between 0.4 and 0.6, and E_{aux} remaining below 1500 kPa. This indicates a consistent mechanical response, suggesting robust and reproducible behavior. In contrast, the *STRI* design displays a broad distribution, reflecting high variability in mechanical performance: E_{aux} reaches up to 4000 kPa, while ε_{aux} spans from near zero to values exceeding 1. The *SREG* design shows similarly high variability in ε_{aux}, reaching up to 1.5 (the widest range among all designs) while maintaining a narrower, more concentrated distribution of E_{aux} that barely exceeds 1000 kPa. This suggests relatively stable stiffness with greater variability in extensibility. Conversely, the *SINV* design demonstrates the opposite trend, with E_{aux} varying widely up to 5000 kPa, and ε_{aux} constrained below 0.5, indicating predictable deformation behavior with less predictable stiffness. These observations highlight how the spread and concentration of each design's mechanical outputs reflect their predictability: narrower distributions imply consistent performance, whereas broader ones indicate greater variability and tunability. The optimal design choice thus depends on the desired trade-off between mechanical stability and adaptability.

Another approach to analyzing the FEM simulation results involved a descriptive exploration of the dataset, focusing on the relationships between geometric parameters ("a", "rba", "d", "yr") and the mechanical outputs (E_{aux}, ε_{aux}) for each scaffold design. This analysis, illustrated in Supp. Info (Figures S2–S5), provides deeper insight into how design-specific geometries influence mechanical performance.

In summary, across all four designs, E_{aux} consistently exhibits a strong dependency on the predictor variables, though the nature of this dependency varies by design. In the *HCELL* configuration, both

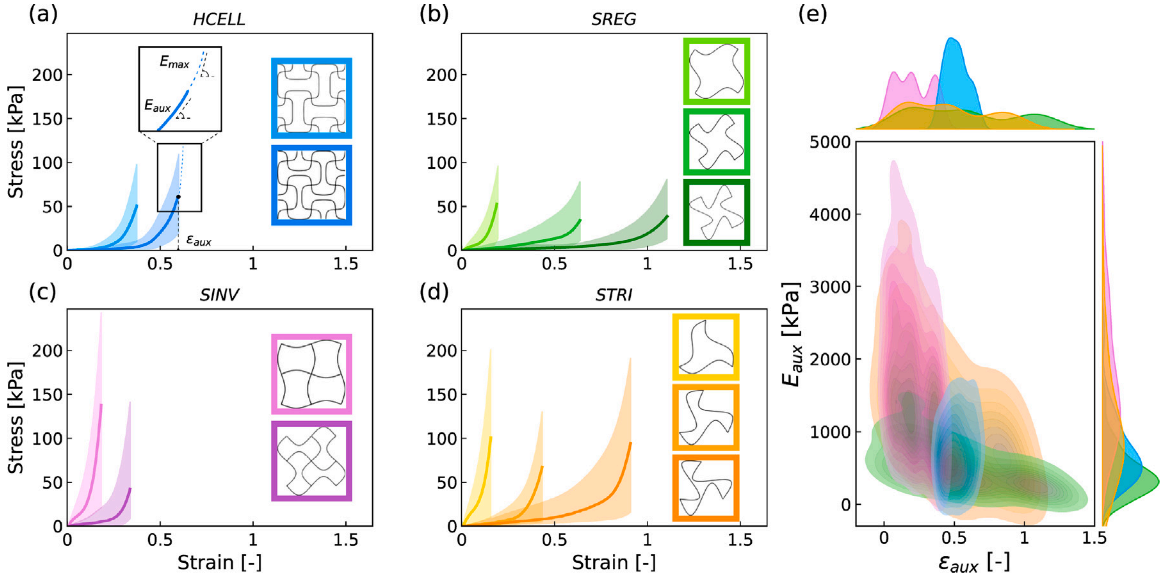

Fig. 3. FEM-based mechanical characterization and design space exploration. (a-d): Simulated stress–strain response for the four auxetic topologies under equibiaxial tensile loading. The curves display a biomimetic non-linear “J-shaped” behavior (initial compliance followed by stiffening). Shaded regions represent the envelopes containing the families of curves obtained from the 81 distinct geometric configurations simulated for each design, demonstrating the wide range of mechanical tunability. (e): Bivariate distribution of the effective stiffness (E_{aux}) versus the auxetic strain limit (ε_{aux}) for each design. The scatter plots highlight the distinct mechanical niches: *SINV* exhibits high stiffness with limited extensibility, whereas *SREG* provides high compliance and large extensibility. The marginal plots display the kernel density estimation, visualizing the probability distribution of properties achievable within the design space.

E_{aux} and $\varepsilon_{\mathrm{aux}}$ display relatively narrow distributions, with moderate sensitivity to all input parameters, suggesting a balanced influence and a robust, predictable mechanical behavior. Notably, increases in “*a*” and “*d*” are associated with reduced/increased stiffness respectively, while “*rba*” exerts a clear inverse influence on strain. The *SREG* design shows a pronounced sensitivity of $\varepsilon_{\mathrm{aux}}$ to the “*rba*” ratio, with strain increasing significantly at higher values, while E_{aux} is most affected by “*a*”, “*rba*” and “*d*”, indicating that structural extensibility is more tunable than stiffness. This is consistent with the broader spread observed in strain outputs for this design, reaching values up to 1.5. In the *SINV* design, $\varepsilon_{\mathrm{aux}}$ remains confined below 0.5 regardless of geometric variations, pointing to limited deformability, with “*rba*” being the only parameter with a clear effect on the achieved strain. On the other hand, E_{aux} is highly responsive to both “*a*” and “*d*”, and to a less extent to “*rba*”, ranging up to 5000 kPa and making this design suitable for applications requiring tunable stiffness with constrained strain. The *STRI* design exhibits the highest overall variability. $\varepsilon_{\mathrm{aux}}$ again shows a dominant dependence on “*rba*”, with strain values spanning a wide range, while E_{aux} responds to a combination of “*a*”, “*d*”, and “*yr*”. This high sensitivity across parameters results in a flexible but less predictable mechanical profile.

An important finding across all designs is the dominant influence of the “*rba*” ratio on the scaffold’s mechanical response, particularly on $\varepsilon_{\mathrm{aux}}$. This parameter, representing the aspect ratio between the primary geometric features of the unit cell, governs the deformation mechanisms underlying auxetic behavior, affecting how the structure expands or contracts laterally under tensile load. By altering the balance between “*a*” and “*b*”, the “*rba*” ratio modulates the kinematic degrees of freedom within the cell, directly impacting both the extent and nature of strain accommodation. Overall, these results highlight how the coupling between design parameters and mechanical responses varies across scaffold architectures. While *HCELL* offers a stable and balanced mechanical response, the other designs, especially *STRI* and *SREG*, enable greater tunability in extensibility, albeit with increased variability.

3.2. Statistical modeling and optimization for target mechanical performance

Statistical regression models were built for each of the four auxetic designs to predict the key mechanical outputs (E_{aux} and $\varepsilon_{\mathrm{aux}}$) based on geometric input parameters from the DOE database. To evaluate the quality of these models, predictions were compared to FEM simulation results for the corresponding geometric configurations. Fig. 4 shows the parity plot for E_{aux}, while the corresponding metrics for $\varepsilon_{\mathrm{aux}}$ can be found in Supp. Info (Figure S6). As shown in Fig. 4, the alignment of the scatter points with the diagonal line reflects a strong agreement between predicted and observed values. Among the models, *SINV* demonstrated the highest accuracy, while *STRI* exhibited greater prediction variability, especially at lower E_{aux} values. In particular, the E_{aux} models exhibited high predictive accuracy across all designs, with Adjusted R^2 values exceeding 0.96. The $\varepsilon_{\mathrm{aux}}$ models showed more variable performance, with higher accuracy for the *HCELL* and *SINV* designs (Adj. $R^2 > 0.99$), and lower accuracy for *SREG* and *STRI* (Adj. $R^2 > 0.82$).

Fig. 4 includes a reference target of 1000 kPa (highlighted by red lines), selected as a representative benchmark across all four scaffold designs. This target lies within the range of output values obtained by the FEM simulations and was used here to neutrally compare the performance of the optimization strategies. By decoupling this initial test from the skin-specific targets addressed later, we ensured a consistent and design-independent basis for evaluating the reliability and efficiency of each method.

To assess the predictive robustness of the regression models near this reference target, a sensitivity analysis was carried out using the *STRI* model, which exhibited the lowest Adj. R^2 value (0.96) and the widest spread between predicted and observed values (see Fig. 4-(d)). This made it a suitable candidate for testing the stability of the optimization pipeline. The analysis involved generating predictions and 95% confidence intervals for all configurations in the *STRI* training dataset (Supp. Info - Figure S7). Comparison with the original FEM outputs revealed several parameter combinations with tight prediction agreement, validating the performance of the model even under moderate variability.

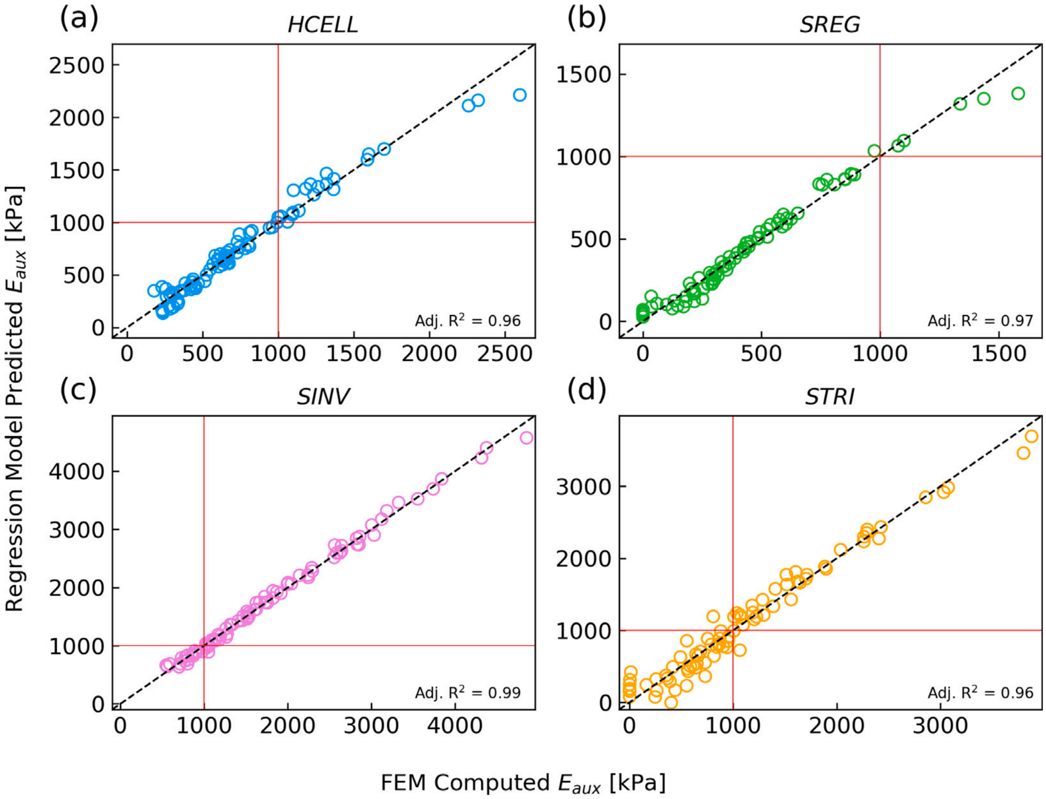

Fig. 4. (a–d): Predictive performance of the regression models. Parity plots comparing the statistically predicted effective stiffness (E_{aux}) against the ground-truth FEM simulation results for the four auxetic designs. The tight alignment of data points along the diagonal ($y = x$) line indicates high accuracy, quantified by Adjusted R^2 values exceeding 0.96 in all cases. The intersecting red lines mark a representative target value of 1000 kPa, utilized here as a neutral benchmark to evaluate the efficiency of the inverse design optimization strategies. The distribution of points relative to this benchmark visualizes the mechanical range of each geometry; for instance, the *SREG* design (b) clusters predominantly below the target, indicating inherently lower stiffness, whereas *SINV* (c) design exhibits a broad distribution exceeding the target, highlighting its suitability for stiffer applications.

Using this 1000 kPa target, we then compared the three previously described optimization strategies: (i) random grid search; (ii) brute-force search and (iii) genetic algorithm. Random grid search emerged as the most efficient method, identifying robust solutions in under 10 s with relatively few evaluations. Brute-force search, while exhaustive and accurate, required substantial computational resources. The genetic algorithm delivered comparable performance to random grid search but offered no advantages in terms of solution quality or runtime and was therefore not selected for further use. A detailed comparison of the three strategies in terms of computational cost and predictive robustness is provided in Supp. Info (Table S1).

This preliminary assessment enabled the selection of an efficient optimization method, which was subsequently applied to achieve target values discussed in the next section.

3.3. Auxetic scaffolds provide reliable solutions to reproduce the behavior of soft tissues

To demonstrate the applicability of the proposed predictive framework, the regression and optimization approach was used to identify auxetic scaffold configurations capable of replicating the mechanical behavior of soft tissues, particularly human skin. Reference values for skin elasticity were obtained from the literature [41], selecting three representative elastic modulus values corresponding to orientations of 90°, 45°, and 0° relative to the local Langer lines. These values ($E(90°) = 725$ kPa, $E(45°) = 1210$ kPa, and $E(0°) = 1580$ kPa) served as target mechanical properties to be matched by the scaffold designs.

For each representative skin modulus, the regression models were employed to predict scaffold geometric configurations that would not only match the target stiffness values but also exhibit stable mechanical behavior. These optimized configurations were subsequently validated through FEM simulations to assess prediction accuracy. Since the FEM framework was experimentally validated [68], it serves as the ground truth for assessing the accuracy of the regression models, eliminating the need for additional physical fabrication in this optimization process. Fig. 5 summarizes the results obtained for the three skin stiffness targets across the four auxetic scaffold designs, including the optimized geometric parameters, predicted and simulated values of E_{aux}, their relative deviations regarding the target, the error between the prediction and the FEM ground truth, and the corresponding predicted and simulated values of $\varepsilon_{\mathrm{aux}}$.

The *HCELL* design showed variable performance across the target range. It delivered reasonable accuracy (5%) for the $E(90°)$ target, but the FEM validation reported larger deviations regarding the target (19%) and the prediction (20%). For the $E(45°)$ target, both predicted and simulated values underestimated the target modulus (deviations between 12% and 15%) but showed good consistency between them (error below 1%). This design struggled to reproduce the higher stiffness value ($E(0°) = 1580$ kPa), with predicted and simulated values falling short (1428 kPa and 1067 kPa, respectively). Nonetheless, predicted and simulated $\varepsilon_{\mathrm{aux}}$ values showed strong agreement across all cases, indicating robust strain estimations.

The *SREG* design achieved excellent accuracy for the lower and intermediate targets ($E(90°)$ and $E(45°)$), with deviations and errors below 10% in both cases. However, it failed to capture the high stiffness target ($E(0°)$), though the consistent correlation between predicted and simulated values across both E_{aux} and $\varepsilon_{\mathrm{aux}}$ supports the model's reliability even when absolute accuracy decreased.

The *SINV* design performed reliably for the intermediate and high targets, providing low-error (below 7%) predictions and simulations for

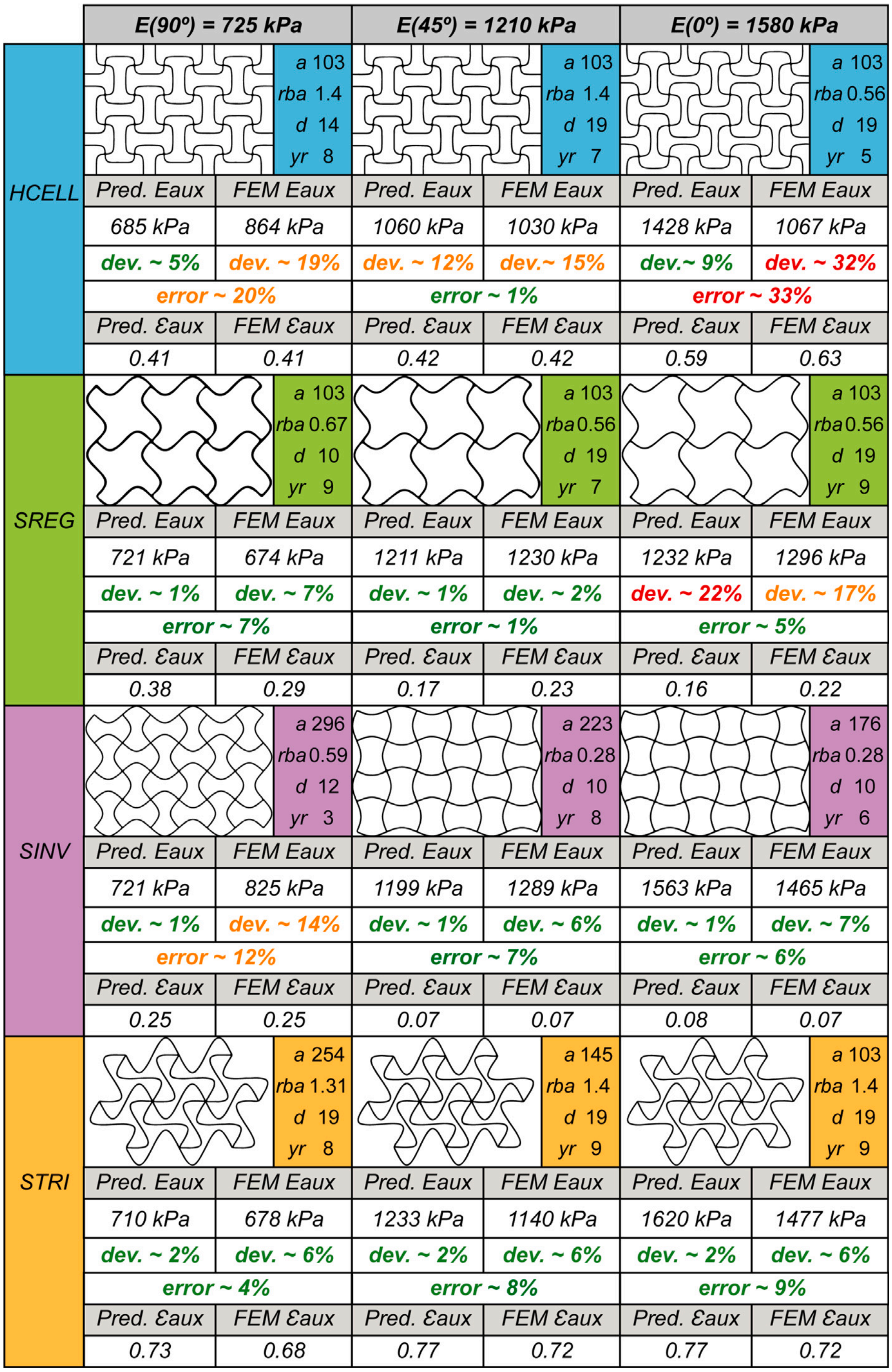

	E(90º) = 725 kPa		E(45º) = 1210 kPa		E(0º) = 1580 kPa	
HCELL		a 103 rba 1.4 d 14 yr 8		a 103 rba 1.4 d 19 yr 7		a 103 rba 0.56 d 19 yr 5
	Pred. Eaux	FEM Eaux	Pred. Eaux	FEM Eaux	Pred. Eaux	FEM Eaux
	685 kPa	864 kPa	1060 kPa	1030 kPa	1428 kPa	1067 kPa
	dev. ~ 5%	dev. ~ 19%	dev. ~ 12%	dev.~ 15%	dev.~ 9%	dev. ~ 32%
	error ~ 20%		error ~ 1%		error ~ 33%	
	Pred. Ɛaux	FEM Ɛaux	Pred. Ɛaux	FEM Ɛaux	Pred. Ɛaux	FEM Ɛaux
	0.41	0.41	0.42	0.42	0.59	0.63
SREG		a 103 rba 0.67 d 10 yr 9		a 103 rba 0.56 d 19 yr 7		a 103 rba 0.56 d 19 yr 9
	Pred. Eaux	FEM Eaux	Pred. Eaux	FEM Eaux	Pred. Eaux	FEM Eaux
	721 kPa	674 kPa	1211 kPa	1230 kPa	1232 kPa	1296 kPa
	dev. ~ 1%	dev. ~ 7%	dev. ~ 1%	dev. ~ 2%	dev. ~ 22%	dev. ~ 17%
	error ~ 7%		error ~ 1%		error ~ 5%	
	Pred. Ɛaux	FEM Ɛaux	Pred. Ɛaux	FEM Ɛaux	Pred. Ɛaux	FEM Ɛaux
	0.38	0.29	0.17	0.23	0.16	0.22
SINV		a 296 rba 0.59 d 12 yr 3		a 223 rba 0.28 d 10 yr 8		a 176 rba 0.28 d 10 yr 6
	Pred. Eaux	FEM Eaux	Pred. Eaux	FEM Eaux	Pred. Eaux	FEM Eaux
	721 kPa	825 kPa	1199 kPa	1289 kPa	1563 kPa	1465 kPa
	dev. ~ 1%	dev. ~ 14%	dev. ~ 1%	dev. ~ 6%	dev. ~ 1%	dev. ~ 7%
	error ~ 12%		error ~ 7%		error ~ 6%	
	Pred. Ɛaux	FEM Ɛaux	Pred. Ɛaux	FEM Ɛaux	Pred. Ɛaux	FEM Ɛaux
	0.25	0.25	0.07	0.07	0.08	0.07
STRI		a 254 rba 1.31 d 19 yr 8		a 145 rba 1.4 d 19 yr 9		a 103 rba 1.4 d 19 yr 9
	Pred. Eaux	FEM Eaux	Pred. Eaux	FEM Eaux	Pred. Eaux	FEM Eaux
	710 kPa	678 kPa	1233 kPa	1140 kPa	1620 kPa	1477 kPa
	dev. ~ 2%	dev. ~ 6%	dev. ~ 2%	dev. ~ 6%	dev. ~ 2%	dev. ~ 6%
	error ~ 4%		error ~ 8%		error ~ 9%	
	Pred. Ɛaux	FEM Ɛaux	Pred. Ɛaux	FEM Ɛaux	Pred. Ɛaux	FEM Ɛaux
	0.73	0.68	0.77	0.72	0.77	0.72

Fig. 5. Validation of the inverse design framework against human skin anisotropy. Comparison between the target elastic modulus and the optimal geometry configurations reported for each auxetic design and target. Each auxetic configuration shows the geometry shape and its parameters, the regression-based E_{aux} prediction, the FEM verification and the error between them, their deviations regarding the specified target, and the predicted and simulated ε_{aux} values. Three targets were selected from literature [41] representing the stiffness of human back skin at distinct orientations relative to Langer lines: 90° (725 kPa), 45° (1210 kPa), and 0° (1580 kPa). The close agreement between predicted and simulated values validates the accuracy of the methodology in generating patient-specific scaffold designs.

$E(45°)$ and $E(0°)$. For the $E(90°)$ target, despite an accurate prediction, FEM simulations revealed greater deviation. This design consistently produced lower strain values (around 0.07) than the other scaffolds (between 0.2 and 0.7), though predicted and simulated ε_{aux} values remained well-aligned.

The *STRI* design demonstrated the most consistent and accurate performance across all three targets. Prediction deviations for E_{aux} remained around 2%, with ground truth errors under 9%, regardless of the target stiffness. ε_{aux} estimations were similarly robust, with close agreement between predicted and simulated values across all configurations.

Overall, these results validate the effectiveness of the predictive framework in identifying scaffold configurations that replicate the mechanical behavior of human skin or other tissues. The distinct performance patterns observed across the different scaffold designs indicate that certain architectures are inherently better suited to achieving specific mechanical targets. This ability to guide targeted scaffold selection represents a meaningful advance in the development of biomimetic auxetic scaffolds for skin tissue engineering applications. To support real-world implementation, we developed a computational tool (described in the following section) that automates the selection and generation of printable scaffold geometries based on target mechanical properties.

3.4. Development of a computational tool for scaffold design optimization and 3D printing

We developed a computational tool [69], including a minimal user interface, that integrates the trained predictive models and optimization algorithms to select optimal parameters and directly generate the corresponding 3D printing or FEM files, streamlining the transition from design to fabrication/simulation and enabling rapid, application-specific scaffold production. This tool allows users to either input specific geometric parameters (Manual Mode) or specify target mechanical properties (Predictive Mode) and automatically obtain the most suitable scaffold geometry.

In the current version, users can input specific values for the geometrical parameters defining the four auxetic designs shown in this work (*HCELL*, *SREG*, *STRI*, and *SINV*) in the “Manual Mode”. Based on these configurations, the platform automatically generates FEM models as ABAQUS input files, G-code files for MEW fabrication, or both. This functionality enables precise control over scaffold design, useful for custom applications or exploratory testing of specific parameter combinations.

In contrast, the “Predictive Mode” encapsulates the core contribution of this study by enabling geometry prediction based on desired mechanical performance. Users are prompted to input a target value for the effective elastic modulus in the toe region, E_{aux}. The pre-trained regression models are then employed to identify the optimal geometric configurations across each of the four auxetic designs. These configurations are subsequently presented in a comparative format, allowing users to assess and select the most appropriate option. As in the “Manual Mode”, the selected configurations can be immediately exported as FEM input files, G-code files, or both, facilitating direct integration into simulation workflows and 3D printing processes.

A block diagram illustrating the functional steps of the computational tool is shown in Fig. 6, outlining the workflow for both modes, by accessing directly to prototype design or starting from mechanical target definition to the generation of design prototypes and exportable files. Supp. Info (Figures S8–S10) includes screenshots of the user interface and example outputs from both design modes, providing a visual reference of the platform in operation.

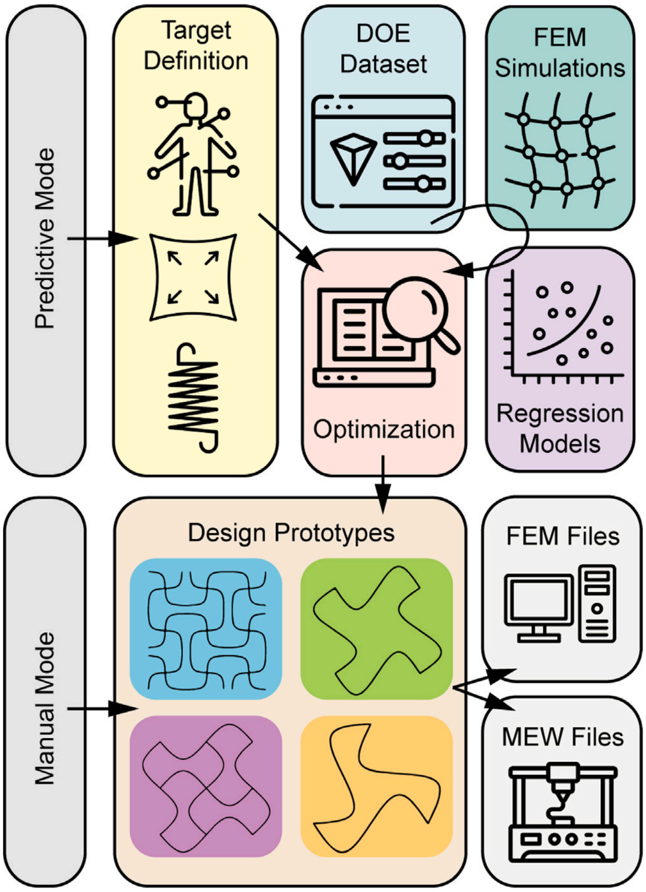

Fig. 6. Operational workflow of the developed computational design software. The diagram illustrates the tool’s architecture, which bridges the gap between theoretical design and fabrication. Two operation modes are available: **(1) Manual Mode**, where users directly define geometric parameters (a, b, d, xr, yr, zr) to explore specific configurations; and **(2) Predictive Mode**, which solves the inverse design problem. In this mode, the user inputs a mechanical target, and the optimization module, powered by the pre-trained regression algorithms, automatically identifies the optimal geometric combination to match that stiffness. Both pathways converge at the generation module, which automatically exports ABAQUS input files for FEM simulation and custom G-code for MEW fabrication, enabling rapid prototyping of patient-specific scaffolds.

4. Discussion

This study establishes an integrated computational framework designed to tailor the mechanical properties of auxetic microfibrous scaffolds, specifically replicating the non-linear behavior of soft tissues like human skin. By integrating finite element simulations with regression-based predictive modeling, we have developed a reliable inverse design methodology capable of identifying scaffold geometries that satisfy precise mechanical targets. This approach reduces the high computational costs associated with traditional iterative design optimization, providing a streamlined and accessible solution for the development of patient-specific tissue engineering scaffolds.

The mechanical characterization of the four auxetic designs (*HCELL*, *SREG*, *SINV*, and *STRI*) revealed distinct behavior patterns that align with the fundamental requirements for skin tissue engineering. All designs exhibited the non-linear “J-curve” stress–strain behavior characteristic of soft tissues, characterized by an initial compliant toe region that transitions into a stiffer linear region under load. This biomimetic response is critical for physiological function, allowing tissues to accommodate small deformations while providing resistance against excessive strain. The remarkable diversity in mechanical performance across the different auxetic designs offers considerable flexibility in addressing the heterogeneous properties of human skin [41]. *SINV* scaffolds demonstrated higher stiffness with limited deformation capacity, making them suitable for applications requiring greater mechanical resilience such as back, chest, or forearms, where skin has stiffer mechanical properties to serve protective functions [37,38,41,78]. In contrast, *SREG* designs exhibited the softest mechanical response with extended deformation capacity, potentially beneficial for more compliant skin regions such as joints or abdomen, which need looser behavior to accommodate frequent movement [78–80]. The *HCELL* and *STRI* designs presented intermediate mechanical behaviors with different degrees of reproducibility and predictability [70].

Analyzing the statistical distribution of E_{aux} and $\varepsilon_{\mathrm{aux}}$ across the design space reveals a critical trade-off between reproducibility and tunability. Narrow distributions, as seen in *HCELL*, imply consistent manufacturing outcomes with reduced sensitivity to geometric deviations. Conversely, designs with broader distributions, such as *SINV* and

STRI, offer a wider dynamic range of achievable mechanical properties, albeit at the cost of potentially lower predictability. This balance between consistency and range must be carefully considered when selecting appropriate designs for specific applications.

The high predictive accuracy of our regression models (Adj. $R^2 > 0.96$ for E_{aux} and Adj. $R^2 > 0.82$ for ε_{aux}) confirms the effectiveness of the proposed approach in reducing reliance on time-intensive FEM simulations during the scaffold design process. Comparison between model predictions and FEM outputs further validates the framework's ability to reliably identify optimal scaffold configurations across diverse mechanical targets. Regarding the optimization strategies, random grid sampling proved to be the most efficient method, delivering robust solutions with minimal computational overhead compared to brute-force or genetic algorithms. Consequently, this algorithm was implemented as the core engine of the computational tool.

When applying our framework to mimic the properties of human skin, we observed varying degrees of success across the different auxetic designs. The *STRI* design demonstrated the most consistent performance across all three skin representative targets (E(90°), E(45°), and E(0°)), with prediction errors around 2% and FEM validation errors around 6%. This consistency indicates the robust adaptability of this particular design across a wide range of stiffness values. The *SINV* design showed excellent performance for intermediate and higher stiffness targets, while *SREG* excelled at lower and intermediate stiffness values. These findings highlight the complementary nature of the different auxetic architectures, effectively expanding the design toolkit available for addressing the diverse mechanical requirements of skin tissue engineering.

The inability of certain designs to accurately reproduce specific target values, particularly the higher stiffness E(0°) target for *HCELL* and *SREG* designs, highlights the inherent limitations of each geometry. This suggests that no single auxetic design can address the full spectrum of skin mechanical properties, emphasizing the importance of a design selection strategy based on specific application requirements. The integration of multiple designs within a single scaffold could potentially provide a more comprehensive mimicry of the complex mechanical behavior of human skin, though this would introduce additional manufacturing challenges.

Our findings align with previous studies that have demonstrated the potential of auxetic materials in tissue engineering applications [2,3,17,19–23]. However, our work extends beyond existing literature by implementing the pipeline in a dedicated software tool that automatically generates scaffold geometries matching a target mechanical response. By providing a full workflow from design space definition to patient-specific scaffold generation, our study establishes a systematic and accessible methodology for predicting and optimizing scaffold properties, and contributes a practical pathway toward translation to tissue engineering applications.

Nevertheless, several limitations should be acknowledged in the current study. First, our framework focuses primarily on the toe and heel regions of the stress–strain curve, characterized by E_{aux} and ε_{aux}. While this region is particularly relevant for capturing the physiological response of skin under normal loading conditions [74], future studies should extend the analysis to include the full non-linear behavior at higher strain levels, especially in applications where tissues are subject to larger deformations.

Second, the current model considers only static mechanical behavior. However, native skin is subjected to dynamic and time-dependent mechanical loading *in vivo*. Incorporating viscoelasticity, time-dependent effects, and fatigue or degradation analysis into the predictive framework would provide a more comprehensive and biologically relevant understanding of scaffold performance under real-world physiological conditions.

Third, our analysis is limited to only four auxetic scaffold architectures. While these architectures were selected to span a range of geometrical features, the design space for auxetic microarchitectures is vast. Expanding the library of tested geometries and integrating more complex or hierarchical structures could unlock novel mechanical behaviors and improve the framework's adaptability across different target tissues. Notably, the developed user interface can serve as a flexible platform for future integration of additional geometries, design rules, or optimization algorithms, enhancing its utility as the methodology evolves.

From a manufacturing perspective, while MEW offers precise control over microfiber deposition, practical fabrication constraints may introduce geometric variations that could influence the scaffold's mechanical performance. Incorporating geometric tolerances into the optimization process would improve the robustness of predicted configurations. In our previous work [68], we explored strategies to minimize these deviations and enhance print fidelity, which could be integrated into future iterations of this computational workflow and reflected in the interface output.

Finally, while mechanical compatibility is a prerequisite for functional tissue engineering, the ultimate success of these constructs depends on their biological integration. Factors such as cell attachment, proliferation, and extracellular matrix deposition are critical. Preliminary studies in our group have demonstrated favorable cell behavior on these scaffolds under *in vitro* conditions; however, comprehensive long-term biological validation is required to assess their viability in a physiological environment [68].

5. Conclusions

In conclusion, this study presents a computational framework that significantly advances the design of auxetic, biomimetic microfibrous scaffolds for skin tissue engineering. By integrating FEM simulations with regression-based predictive modeling and optimization strategies, we established a methodology capable of efficiently identifying scaffold geometries tailored to specific mechanical targets. The distinct performance of each auxetic design across the stiffness spectrum highlights the versatility of the framework in addressing the heterogeneous and anisotropic properties of human skin.

The results demonstrate that the proposed inverse design methodology can accurately identify optimal scaffold geometries that match patient-specific mechanical targets without the need for iterative trial-and-error fabrication. Furthermore, the validation of the regression models against the high-fidelity FEM "digital twin" confirmed the reliability of this approach for exploring complex design landscapes.

A key contribution of this work is the translation of these findings into a user-friendly software tool. This application bridges the gap between theoretical metamaterial design and clinical utility, empowering bioengineers and clinicians to generate custom scaffold architectures based simply on target mechanical inputs. Collectively, this integrated workflow significantly advances the field of personalized regenerative medicine, offering a scalable and efficient path for designing mechanically compatible tissue substitutes.

Ultimately, this approach not only reduces computational demands but also provides a systematic and accessible path for scaffold design based on desired mechanical outcomes. Future work should focus on the experimental validation of the optimized configurations, in-depth investigation of cell-scaffold interactions, and the incorporation of additional factors such as dynamic loading, viscoelastic behavior, and biological cues relevant to skin tissue regeneration.

CRediT authorship contribution statement

Óscar Lecina-Tejero: Writing – review & editing, Writing – original draft, Software, Investigation. **Jesús Asín:** Writing – review & editing, Supervision, Methodology. **Jesús Cuartero:** Supervision, Resources, Methodology. **María Ángeles Pérez:** Writing – review & editing, Supervision, Methodology, Investigation. **Carlos Borau:** Writing – review & editing, Supervision, Software, Methodology, Investigation.

Declaration of competing interest

The authors declare that they have no known competing financial interests or personal relationships that could have appeared to influence the work reported in this paper.

Acknowledgments

Authors would like to acknowledge the Spanish Ministry of Economy and Competitiveness through the projects PID2023-146072OB-I00 and PID2024-155426OB-I00; and Gobierno de Aragón, Spain under Research Group E46_23R: Modelos Estocásticos. C.B. is funded by a Ramon & Cajal Fellowship (RYC2023-042524-I funded by MICIU/AEI/10.13039/501100011033 and the European Social Fund Plus).

Appendix A. Supplementary data

Supplementary material related to this article can be found online at https://doi.org/10.1016/j.ijmecsci.2026.111251.

Data availability

We have shared the codes developed and the software tool in GitHub: https://github.com/olecina/MEW-FEM-AuxeticDesigner.

References

[1] Tavakoli S, Klar AS. Bioengineered skin substitutes: Advances and future trends. Appl Sci 2021;11(4):1493. http://dx.doi.org/10.3390/app11041493.

[2] Sharmin T, Shirwaiker R. Assessing design-induced elasticity of 3D printed auxetic scaffolds for tissue engineering applications. Manuf Lett 2024;41:780–6. http://dx.doi.org/10.1016/j.mfglet.2024.09.097.

[3] Jang K, Chung H, Xu S, et al. Soft network composite materials with deterministic and bio-inspired designs. Nat Commun 2015;6:6566. http://dx.doi.org/10.1038/ncomms7566.

[4] Mir M, Ali MN, Sami J, Ansari U. Review of mechanics and applications of auxetic structures. Adv Mater Sci Eng 2014;753496. http://dx.doi.org/10.1155/2014/753496, 17 pages.

[5] Kim Y, Son KH, Lee JW. Auxetic structures for tissue engineering scaffolds and biomedical devices. Materials 2021;14(22):6821. http://dx.doi.org/10.3390/ma14226821.

[6] Mardling P, Alderson A, Jordan-Mahy N, Le Maitre CL. The use of auxetic materials in tissue engineering. Biomater Sci 2020;8:2074–83. http://dx.doi.org/10.1039/C9BM01928F.

[7] Chen K, Wu L, Wang G, Li Z, Zhao C, Xu T. Application of negative Poisson's ratio metamaterials in medical field: a comprehensive review. Funct Compos Struct 2025;7:032001. http://dx.doi.org/10.1088/2631-6331/ade758.

[8] Sun M, Hu X, Tian L, Yang X, Min L. Auxetic biomedical metamaterials for orthopedic surgery applications: A comprehensive review. Orthop Surg 2024;16(8):1801–15. http://dx.doi.org/10.1111/os.14142.

[9] Geng X, Yao Y, Huang H, Li Q, Wang L, Fan Y. Mechanical and biological characteristics of 3D-printed auxetic structure in bone tissue engineering. J Biomech 2025;184:112685. http://dx.doi.org/10.1016/j.jbiomech.2025.112685.

[10] Chen X, Liu C, Wadsworth M, Zeng EZ, Driscoll T, Zeng C, Li Y. Surface engineering of auxetic scaffolds for neural and vascular differentiation from human pluripotent stem cells. Adv Heal Mater 2023;12(6):2202511. http://dx.doi.org/10.1002/adhm.202202511.

[11] Song L, Ahmed MF, Li Y, Zeng C, Li Y. Vascular differentiation from pluripotent stem cells in 3-D auxetic scaffolds. J Tissue Eng Regen Med 2018;12(7):1679–89. http://dx.doi.org/10.1002/term.2695.

[12] Paxton NC, Daley R, Forrestal DP, Allenby MC, Woodruff MA. Auxetic tubular scaffolds via melt electrowriting. Mater Des 2020;193:108787. http://dx.doi.org/10.1016/j.matdes.2020.108787.

[13] Chen Y, Arzani M, Mu X, Jin S, Xiao S. Mechanics and design of metastructured auxetic patches with bio-inspired materials. Appl Phys A 2025;131:540. http://dx.doi.org/10.1007/s00339-025-08655-z.

[14] Kapnisi M, Mansfield C, Marijon C, Guex AG, Perbellini F, Bardi I, Humphrey EJ, Puetzer JL, Mawad D, Koutsogeorgis DC, et al. Auxetic cardiac patches with tunable mechanical and conductive properties toward treating myocardial infarction. Adv Funct Mater 2018;28(21):1800618. http://dx.doi.org/10.1002/adfm.201800618.

[15] Brazhkina O, Park JH, Park H-J, Bheri S, Maxwell JT, Hollister SJ, Davis ME. Designing a 3D printing based auxetic cardiac patch with hiPSC-CMs for heart repair. J Cardiovasc Dev Dis 2021;8(12):172. http://dx.doi.org/10.3390/jcdd8120172.

[16] Dong Z, Ren X, Jia B, Zhang X, Wan X, Wu Y, Huang H. Composite patch with negative Poisson's ratio mimicking cardiac mechanical properties: Design, experiment and simulation. Mater Today Bio 2024;26:101098. http://dx.doi.org/10.1016/j.mtbio.2024.101098.

[17] Mirani B, Mathew SO, Latifi N, Labrosse MR, Amsden BG, Simmons CA. Programmable melt electrowriting to engineer soft connective tissues with prescribed, biomimetic, biaxial mechanical properties. Adv Funct Mater 2024;34:2302786. http://dx.doi.org/10.1002/adfm.202302786.

[18] Shukla S, Behera B. Auxetic fibrous materials and structures in medical engineering–a review. J Text Inst 2023;114(7):1078–89. http://dx.doi.org/10.1080/00405000.2022.2116549.

[19] Óscar Lecina-Tejero, Ángeles Pérez M, García-Gareta E, Borau C. The rise of mechanical metamaterials: Auxetic constructs for skin wound healing. J Tissue Eng 2023;14. http://dx.doi.org/10.1177/20417314231177838.

[20] Flamourakis G, Spanos I, Vangelatos Z, Manganas P, Papadimitriou L, Grigoropoulos C, Ranella A, Farsari M. Laser-made 3D auxetic metamaterial scaffolds for tissue engineering applications. Macromol Mater Eng 2020;305(7):2000238. http://dx.doi.org/10.1002/mame.202000238.

[21] Jin Y, Xie C, Gao Q, Zhou X, Li G, Du J, He Y. Fabrication of multi-scale and tunable auxetic scaffolds for tissue engineering. Mater Des 2021;197:109277. http://dx.doi.org/10.1016/j.matdes.2020.109277.

[22] Lvov VA, Senatov FS, Veveris AA, Skrybykina VA, Díaz Lantada A. Auxetic metamaterials for biomedical devices: Current situation, main challenges, and research trends. Materials 2022;15(4):1439. http://dx.doi.org/10.3390/ma15041439.

[23] Chansoria P, Blackwell J, Etter EL, Bonacquisti EE, Jasiewicz N, Neal T, Kamal SA, Hoque J, Varghese S, Egan T, et al. Rationally designed anisotropic and auxetic hydrogel patches for adaptation to dynamic organs. Adv Funct Mater 2022;32(43):2207590. http://dx.doi.org/10.1002/adfm.202207590.

[24] Holzapfel GA, Humphrey JD, Ogden RW. Biomechanics of soft biological tissues and organs, mechanobiology, homeostasis and modelling. J R Soc Interface 2025;22(222):20240361. http://dx.doi.org/10.1098/rsif.2024.0361.

[25] Tejo-Otero A, Fenollosa-Artés F, Achaerandio I, Rey-Vinolas S, Buj-Corral I, Mateos-Timoneda MÁ, Engel E. Soft-tissue-mimicking using hydrogels for the development of phantoms. Gels 2022;8(1):40. http://dx.doi.org/10.3390/gels8010040.

[26] Wang Z, Jiang F, Zhang Y, You Y, Wang Z, Guan Z. Bioinspired design of nanostructured elastomers with cross-linked soft matrix grafting on the oriented rigid nanofibers to mimic mechanical properties of human skin. ACS Nano 2015;9(1):271–8. http://dx.doi.org/10.1021/nn506960f.

[27] Ceylan S, Demir D, Harris C, İpek SL, Vavourakis V, Manca M, Dubrac S, Bauer R. Skin in the game: a review of computational models of the skin. BioData Min 2025;18(1):55. http://dx.doi.org/10.1186/s13040-025-00471-8.

[28] Hussain SH, Limthongkul B, Humphreys TR. The biomechanical properties of the skin. Dermatol Surg 2013;39(2):193–203. http://dx.doi.org/10.1111/dsu.12095.

[29] Limbert G. Mathematical and computational modelling of skin biophysics: a review. Proc R Soc A: Math Phys Eng Sci 2017;473(2203):20170257. http://dx.doi.org/10.1098/rspa.2017.0257.

[30] Low ZWK, Li Z, Owh C, Chee PL, Ye E, Kai D, Yang D-P, Loh XJ. Using artificial skin devices as skin replacements: insights into superficial treatment. Small 2019;15(9):1805453. http://dx.doi.org/10.1002/smll.201805453.

[31] Singh G, Gupta V, Chanda A. Artificial skin with varying biomechanical properties. Mater Today: Proc 2022;62:3162–6. http://dx.doi.org/10.1016/j.matpr.2022.03.433.

[32] Bian S, Hu X, Zhu H, Du W, Wang C, Wang L, Hao L, Xiang Y, Meng F, Hu C, et al. 3D bioprinting of artificial skin substitute with improved mechanical property and regulated cell behavior through integrating patterned nanofibrous films. ACS Nano 2024;18(28):18503–21. http://dx.doi.org/10.1021/acsnano.4c04088.

[33] Lei Z, Wu P. A supramolecular biomimetic skin combining a wide spectrum of mechanical properties and multiple sensory capabilities. Nat Commun 2018;9(1):1134. http://dx.doi.org/10.1038/s41467-018-03456-w.

[34] Chanda A. Biomechanical modeling of human skin tissue surrogates. Biomimetics 2018;3(3):18. http://dx.doi.org/10.3390/biomimetics3030018.

[35] Veronda DR, Westmann RA. Mechanical characterization of skin—Finite deformations. J Biomech 1970;3:111–22. http://dx.doi.org/10.1016/0021-9290(70)90055-2.

[36] Lees C, Vincent JFV, Hillerton JE. Poisson's ratio in skin. Bio-Medical Mater Eng 1991;1(1):19–23. http://dx.doi.org/10.3233/BME-1991-1104.

[37] Agache PG, Monneur C, Leveque JL, De Rigal J. Mechanical properties and Young's modulus of human skin in vivo. Arch Dermatol Res 1980;269:221–32. http://dx.doi.org/10.1007/BF00406415.

[38] Pissarenko A, Meyers MA. The materials science of skin: Analysis, characterization, and modeling. Prog Mater Sci 2020;110:100634. http://dx.doi.org/10.1016/j.pmatsci.2019.100634.

[39] Dwivedi KK, Lakhani P, Kumar S, Kumar N. Effect of collagen fibre orientation on the Poisson's ratio and stress relaxation of skin: an ex vivo and in vivo study. R Soc Open Sci 2022;9:211301. http://dx.doi.org/10.1098/rsos.211301.

[40] Pawlaczyk M, Lelonkiewicz M, Wieczorowski M. Age-dependent biomechanical properties of the skin. Adv Dermatol Allergology/Postępy Dermatol I Alergol 2013;30(5):302–6. http://dx.doi.org/10.5114/pdia.2013.38359.

[41] Ní Annaidh A, Bruyère K, Destrade M, Gilchrist MD, Otténio M. Characterization of the anisotropic mechanical properties of excised human skin. J Mech Behav Biomed Mater 2012;5:139–48. http://dx.doi.org/10.1016/j.jmbbm.2011.08.016.

[42] Pomerantz ER, Griffin NL, Brownstone ND. Clarifying the role of skin tension lines in dermatological surgery. Dermatol Online J 2025;31(2). http://dx.doi.org/10.5070/D331265288.

[43] Carmichael SW. The tangled web of Langer's lines. Clin Anat 2014;27(2):162–8. http://dx.doi.org/10.1002/ca.22278.

[44] Abyaneh M-AY, Griffith R, Falto-Aizpurua L, Nouri K. Famous lines in history: Langer lines. JAMA Dermatol 2014;150(10). http://dx.doi.org/10.1001/jamadermatol.2014.659, 1087–1087.

[45] Castilho M, van Mil A, Maher M, Metz CHG, Hochleitner G, Groll J, Doevendans PA, Ito K, Sluijter JPG, Malda J. Melt electrowriting allows tailored microstructural and mechanical design of scaffolds to advance functional human myocardial tissue formation. Adv Funct Mater 2018;28:1803151. http://dx.doi.org/10.1002/adfm.201803151.

[46] Castilho M, Mouser V, Chen M, Malda J, Ito K. Bi-layered micro-fibre reinforced hydrogels for articular cartilage regeneration. Acta Biomater 2019;95:297–306. http://dx.doi.org/10.1016/j.actbio.2019.06.030.

[47] Zhang X, Xu Z, Qiao Z, Wang H, Peng L, Dai K. Highly architectural MEW scaffolds with superior performance. Mater Des 2024;245:113290.

[48] Jin Y, Gao Q, Xie C, Li G, Du J, Fu J, He Y. Fabrication of heterogeneous scaffolds using melt electrospinning writing: Design and optimization. Mater Des 2020;185:108274. http://dx.doi.org/10.1016/j.matdes.2019.108274.

[49] Loewner S, Heene S, Baroth T, Heymann H, Cholewa F, Blume H, Blume C. Recent advances in melt electro writing for tissue engineering for 3D printing of microporous scaffolds for tissue engineering. Front Bioeng Biotechnol 2022;10:896719. http://dx.doi.org/10.3389/fbioe.2022.896719.

[50] Yin Y, Yang H, Han W, Guo C, Mu Q, Yang H, Chen D. Melt electrowriting for biomimetic tissue engineering: advances in scaffold design, materials, and multifunctional applications. Polym Adv Technol 2025;36(1):e70067. http://dx.doi.org/10.1002/pat.70067.

[51] Snow F, Doyle SE, Liu E, De Rauch D, Millett D, Wilding-Mcbride J, Kita M, Pirogova E, Kapsa RMI, Quigley A. A detailed guide to melt electro-writing for tissue engineering applications. Biofabrication 2025;17(4):042004. http://dx.doi.org/10.1088/1758-5090/adfbc4.

[52] Girard F, Lajoye C, Camman M, Tissot N, Berthelot Pedurand F, Tandon B, Moedder D, Liashenko I, Salameh S, Dalton PD, et al. First advanced bilayer scaffolds for tailored skin tissue engineering produced via electrospinning and melt electrowriting. Adv Funct Mater 2024;34(27):2314757. http://dx.doi.org/10.1002/adfm.202314757.

[53] Liu J, Zhang Y. Soft network materials with isotropic negative Poisson's ratios over large strains. Soft Matter 2018;14(5):693–703. http://dx.doi.org/10.1039/C7SM02052J.

[54] Ghavidelnia N, Bodaghi M, Hedayati R. Idealized 3D auxetic mechanical metamaterial: an analytical, numerical, and experimental study. Materials 2021;14(4):993. http://dx.doi.org/10.3390/ma14040993.

[55] Liu H, Ahlinder A, Yassin MA, Finne-Wistrand A, Gasser TC. Computational and experimental characterization of 3D-printed PCL structures toward the design of soft biological tissue scaffolds. Mater Des 2020;188:108488. http://dx.doi.org/10.1016/j.matdes.2020.108488.

[56] Chen J, Wei Z, Xiao X, Wei K, Yang X, Qu Z, Fang D. Mining extreme properties from a large metamaterial database. Nat Commun 2025;16:9648. http://dx.doi.org/10.1038/s41467-025-64745-9.

[57] Cerniauskas G, Sadia H, Alam P. Machine intelligence in metamaterials design: a review. Oxf Open Mater Sci 2024;4(1):itae001. http://dx.doi.org/10.1093/oxfmat/itae001.

[58] Song J, Lee J, Kim N, Min K. Artificial intelligence in the design of innovative metamaterials: A comprehensive review. Int J Precis Eng Manuf 2024;25(1):225–44. http://dx.doi.org/10.1007/s12541-023-00857-w.

[59] He L, Li Y, Torrent D, Zhuang X, Rabczuk T, Jin Y. Machine learning assisted intelligent design of meta structures: a review. Microstructures 2023;3(4):N–A. http://dx.doi.org/10.20517/microstructures.2023.29.

[60] Zhang C, Zhao YF. A critical review on the application of machine learning in supporting auxetic metamaterial design. J Phys: Mater 2024;7(2):022004. http://dx.doi.org/10.1088/2515-7639/ad33a4.

[61] Wilt JK, Yang C, Gu GX. Accelerating auxetic metamaterial design with deep learning. Adv Eng Mater 2020;22(5):1901266. http://dx.doi.org/10.1002/adem.201901266.

[62] Li W, Chen P, Xiong B, Liu G, Dou S, Zhan Y, Zhu Z, Chu T, Li Y, Ma W. Deep learning modeling strategy for material science: from natural materials to metamaterials. J Phys: Mater 2022;5(1):014003. http://dx.doi.org/10.1088/2515-7639/ac5914.

[63] Zheng X, Zhang X, Chen T-T, Watanabe I. Deep learning in mechanical metamaterials: from prediction and generation to inverse design. Adv Mater 2023;35(45):2302530. http://dx.doi.org/10.1002/adma.202302530.

[64] Zheng X, Chen T-T, Guo X, Samitsu S, Watanabe I. Controllable inverse design of auxetic metamaterials using deep learning. Mater Des 2021;211:110178. http://dx.doi.org/10.1016/j.matdes.2021.110178.

[65] Chang Y, Wang H, Dong Q. Machine learning-based inverse design of auxetic metamaterial with zero Poisson's ratio. Mater Today Commun 2022;30:103186. http://dx.doi.org/10.1016/j.mtcomm.2022.103186.

[66] Bessa MA, Glowacki P, Houlder M. Bayesian machine learning in metamaterial design: Fragile becomes supercompressible. Adv Mater 2019;31(48):1904845. http://dx.doi.org/10.1002/adma.201904845.

[67] Bessa M, Bostanabad R, Liu Z, Hu A, Apley D, Brinson C, Chen W, Liu W. A framework for data-driven analysis of materials under uncertainty: Countering the curse of dimensionality. Comput Methods Appl Mech Engrg 2017;320:1. http://dx.doi.org/10.1016/j.cma.2017.03.037.

[68] Lecina-Tejero Ó, Iamsamang J, Alamán-Díez P, García-Gareta E, Cuartero J, Pérez M, Miguel C, Borau C. Rational design and modeling of auxetic fiber scaffolds for soft tissue engineering via melt electrowriting. Results Eng 2025;28:107001. http://dx.doi.org/10.1016/j.rineng.2025.107001.

[69] Lecina-Tejero Ó, Asín J, Iamsamang J, Cuartero J, Castilho M, Pérez M, Borau C. MEW-FEM-AuxeticDesigner. 2025, http://dx.doi.org/10.5281/zenodo.15516602.

[70] Devlin BL, Pickering E, Allenby MC, Paxton NC, Woodruff MA. Advancing scaffold biomimicry: engineering mechanics in microfiber scaffolds with independently controlled architecture using melt electrowriting. 2023, http://dx.doi.org/10.1101/2023.05.28.542676, BioRxiv.

[71] Devlin BL, Kuba S, Hall PC, McCosker AB, Pickering E, Dalton PD, Klein TJ, Woodruff MA. A melt electrowriting toolbox for automated G-code generation and toolpath correction of flat and tubular constructs. Adv Mater Technol 2024;9:2400419. http://dx.doi.org/10.1002/admt.202400419.

[72] Liashenko I, Hrynevich A, Dalton PD. Designing outside the box: Unlocking the geometric freedom of melt electrowriting using microscale layer shifting. Adv Mater 2020;32:2001874. http://dx.doi.org/10.1002/adma.202001874.

[73] Lecina-Tejero Ó, Iamsamang J, Alamán-Díez P, Garcia-Gareta E, Cuartero J, Pérez M, Castilho M, Borau Zamora C. Dataset: Advancing skin tissue engineering through computational design and fabrication of auxetic fiber scaffolds via melt electrowriting. 2025, http://dx.doi.org/10.5281/zenodo.14966964.

[74] Huang H-YS, Huang S, Frazier CP, Prim PM, Harrysson O. Directional biomechanical properties of porcine skin tissue. J Mech Med Biol 2014;14(05):1450069. http://dx.doi.org/10.1142/S0219519414500699.

[75] Vignali S, Barras AG, Arlettaz R, Braunisch V. SDMtune: An r package to tune and evaluate species distribution models. Ecol Evol 2020;10(20):11488–506. http://dx.doi.org/10.1002/ece3.6786.

[76] Bhat PC, Prosper HB, Sekmen S, Stewart C. Optimizing event selection with the random grid search. Comput Phys Comm 2018;228:245–57. http://dx.doi.org/10.1016/j.cpc.2018.02.018.

[77] Scrucca L. GA: A package for genetic algorithms in R. J Stat Softw 2013;53(4):1–37. http://dx.doi.org/10.18637/jss.v053.i04.

[78] Wong VW, Beasley B, Zepeda J, Dauskardt RH, Yock PG, Longaker MT, Gurtner GC. A mechanomodulatory device to minimize incisional scar formation. Adv Wound Care 2013;2(4):185–94. http://dx.doi.org/10.1089/wound.2012.0396.

[79] Yazdi SJM, Baqersad J. Mechanical modeling and characterization of human skin: A review. J Biomech 2022;130:110864. http://dx.doi.org/10.1016/j.jbiomech.2021.110864.

[80] Park J-K, Kim KW, Kim HJ, Choi SY, Son KH, Lee JW. 3D-printed auxetic skin scaffold for decreasing burn wound contractures at joints. J Funct Biomater 2023;14(10):516. http://dx.doi.org/10.3390/jfb14100516.